

PHD TUTORIAL

A small trapped-ion quantum register

D KielpinskiResearch Laboratory of Electronics and Center for Ultracold Atoms,
Massachusetts Institute of Technology, Cambridge, MA 02139, USA

Received 4 August 2002, in final form 19 February 2003

Published 10 April 2003

Online at stacks.iop.org/JOptB/5/R121**Abstract**

We review experiments performed at the National Institute of Standards and Technology on entanglement, Bell's inequality and decoherence-free subspaces (DFSs) in a quantum register of trapped ${}^9\text{Be}^+$ ions. The group of Dr David Wineland has demonstrated entanglement of up to four ions using the technique of Mølmer and Sørensen. This method produces the state $(|\downarrow\downarrow\rangle + |\uparrow\uparrow\rangle)/\sqrt{2}$ for two ions and the state $(|\downarrow\downarrow\downarrow\downarrow\rangle + |\uparrow\uparrow\uparrow\uparrow\rangle)/\sqrt{2}$ for four ions. The entanglement was generated deterministically in each shot of the experiment. Measurements on the two-ion entangled state violate Bell's inequality at the 8σ level. Because of the high detector efficiency of the apparatus, this experiment closes the detector loophole for Bell's inequality measurements for the first time. This measurement is also the first violation of Bell's inequality by massive particles that does not implicitly assume results from quantum mechanics. The group also demonstrated measurement of an interferometric phase with precision better than the shot-noise limit using a two-ion entangled state. A large-scale version of this scheme could improve the signal-to-noise ratio of atomic clocks by orders of magnitude. Further experiments demonstrated reversible encoding of an arbitrary qubit, originally contained in one ion, into a DFS of two ions. The DFS-encoded qubit resists applied collective dephasing noise and retains coherence under ambient conditions 3.6 times longer than does an unencoded qubit. The encoding method, which uses single-ion gates and the two-ion entangling gate, demonstrates all the elements required for two-qubit universal quantum logic. Finally, we describe an architecture for a large-scale ion trap quantum computer. By performing logic gates on small numbers of ions trapped in separate regions of the array, we take advantage of existing techniques for manipulating small trapped-ion quantum registers while enabling massively parallel gate operation. Encoding the quantum information in the DFS removes decoherence associated with ion transport and imperfect clock synchronization.

Keywords: Quantum information, entanglement, decoherence, error correction, cooling, quantum optics

(Some figures in this article are in colour only in the electronic version)

1. Introduction

This paper describes the construction of a small quantum register at the National Institute of Standards and Technology (NIST) using laser-cooled ${}^9\text{Be}^+$ ions in a linear RF trap. Most of the work described here was performed during the

author's PhD study in the group of Dr David Wineland, and the use of 'we' should be taken to refer to the efforts of that group. The quantum register is composed of elementary two-level systems, 'qubits', which are analogous to single bits in a classical computer. Each qubit corresponds to a single trapped ion, with the two-qubit levels being two hyperfine

sublevels of the ground electronic state. The quantum state of the whole register encodes information, and an appropriate unitary evolution of the state of the register can perform a computing task.

Trapped ions are a promising candidate system for implementing quantum computing (QC), with potential applications like efficient factorization of large numbers [1] and efficient searching of large databases [2]. While large-scale QC is still far off, trapped-ion quantum registers have already demonstrated all the essential ingredients of QC, including initialization to a known quantum state [3–5], efficient detection of final states [5, 6], long qubit coherence times [7–9] and a universal set of quantum logic gates [5, 10–12]. In some sense, then, only technical difficulties stand between us and a full-scale quantum computer, and we have presented a scheme for overcoming these difficulties [13]. For some tasks, quantum algorithms are much more efficient than any known classical algorithm, in particular for factoring of large numbers [1]. To factor an N -digit number, a classical computer requires resources that are exponential in N , but a quantum computer only requires resources polynomial in N . Because most modern cryptography relies on the difficulty of factoring large numbers, a full-scale quantum computer could have a large impact on many areas of technology, internet commerce being only one example.

We used the quantum register to study two central phenomena in quantum information: entanglement and decoherence. Writing the two states of a qubit as $|\downarrow\rangle$ and $|\uparrow\rangle$, we see that the two-qubit state $|\downarrow\uparrow\rangle - |\uparrow\downarrow\rangle$ is entangled: we cannot decompose this state into a product $|\Psi_1\rangle|\Psi_2\rangle$ of two single-qubit states. While quantum logic operations on single qubits have been commonplace for a long time under a variety of names, controlled manipulation of entanglement has only become possible in the last few years. Entanglement is thought to be closely related to the efficiency of quantum computers. A unique feature of our experiment is that we can generate and manipulate entangled states of two qubits on demand, so that we have complete control over the behaviour of the register. No other QC experiment has demonstrated this ability to date. We used entangled states of two ions to observe violation of Bell’s inequality [6] and to measure interferometric phase with sub-shot-noise precision [14].

If entanglement provides the power of QC, decoherence takes it away again. Interactions of our quantum register with the environment disturb the register state, causing transfer of the information in the register to the environment. From the quantum information point of view, decoherence is just this loss of information from the register. A wide variety of physical processes cause decoherence, and methods of eliminating decoherence will be essential for large-scale quantum computers. We demonstrated encoding of quantum information into a decoherence-free subspace (DFS). The encoded information resisted a wide variety of decoherence processes, and survived much longer than the unencoded information under ambient conditions. The useful properties of the encoding suggest that some similar encoding will be commonly used in large-scale QC.

The small ion-trap quantum register described here is only the first step toward large-scale QC. We propose a scheme, based on interconnected ion traps, that uses only operations that

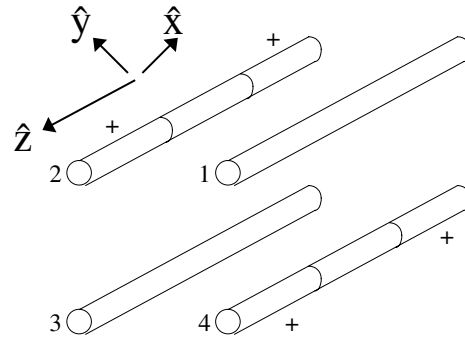


Figure 1. Electrode structure of a linear RF trap. A common RF voltage is applied to rods 1 and 3, while rods 2 and 4 are held at RF ground. Rods 1 and 3 are held at DC ground, while the ‘endcap’ segments of rods 2 and 4, labelled with a ‘+’, are held at positive DC potential with respect to the middle segments of those rods.

have already been demonstrated in small registers. Using the DFS encoding, we can eliminate errors due to ion transport and imperfect synchronization between traps, greatly improving the feasibility of the scheme.

2. Ion traps for QC

All experiments in ion-trap QC so far have used radio-frequency (RF) traps to confine ions under ultra-high vacuum. In these traps, one applies large RF voltages to an electrode structure made of conducting material in order to create a quadrupole electric field with a minimum in free space. For appropriate RF voltages and frequencies, the RF field induces a ponderomotive potential that confines ions harmonically at the field minimum. The ions are then well isolated from environmental perturbations, enabling the precise quantum state control needed for these experiments.

Linear RF traps were used for almost all the experiments described here. One common electrode structure for such a trap [15] is shown in figure 1. Essentially the trap is a quadrupole mass filter plugged at the ends with static potentials. To operate the trap, one applies RF voltage to rods 1 and 3 of figure 1, while rods 2 and 4 are held at RF ground. The induced ponderomotive potential [16] confines the ions to the RF nodal line, which lies along the \hat{z} axis. The ‘endcap’ segments of rods 2 and 4 are held at a positive DC voltage relative to the middle segments of those rods, pushing the (positive) ions toward the centre of the trap. For motional amplitudes characteristic of laser-cooled ions, the resulting trap potential is harmonic in all three directions, with trap frequencies up to tens of MHz.

When multiple ions are present in the trap, one must consider the Coulomb repulsion between ions as well as the ions’ interaction with the harmonic trapping potential. If the ions are sufficiently cold, the classical equilibrium positions of the ions are given by minimizing the potential energy. For sufficiently weak axial confinement, the equilibrium positions all lie on the trap axis $x = y = 0$, so that the ions line up in a string, as shown in figure 2. Minimizing the combined trap and Coulomb potential gives the equilibrium positions along the axis [17–19]. For two and four ions, the cases of interest here, the scaled positions are given in table 1. Here the scaling factor $\ell = 25(\omega_z/10^6)^{-2/3} \mu\text{m}$ for ${}^9\text{Be}^+$, with ω_z the axial trap frequency in rad s^{-1} .

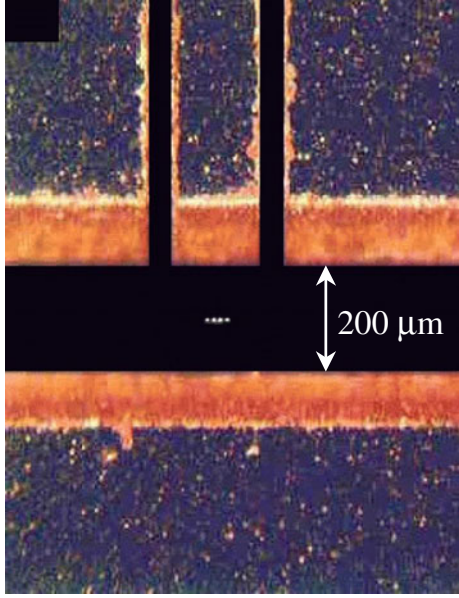


Figure 2. A string of four ions in the linear trap.

Table 1. Positions for two and four ions, in units of ℓ (see text).

N	Position			
2	$-(1/2)^{2/3}$	$(1/2)^{2/3}$		
4	-1.437	-0.454	0.454	1.437

Table 2. Normal modes of motion along \hat{z} for linear crystals of two and four ions. Frequencies ξ_k are given in units of ω_z . Eigenvectors $\vec{v}^{(k)}$ are orthonormal.

N	ξ_k	$\vec{v}^{(k)}$				Name
2	1	$1/\sqrt{2}$	$1/\sqrt{2}$			COM
	$\sqrt{3}$	$-1/\sqrt{2}$	$1/\sqrt{2}$			Stretch
4	1	1/2	1/2	1/2	1/2	COM
	$\sqrt{3}$	-0.674	-0.213	0.213	0.674	Stretch 1
	2.41	1/2	-1/2	-1/2	1/2	Stretch 2
	3.05	-0.213	0.674	-0.674	0.213	Stretch 3

After laser cooling, the residual motion of the ions is very small, so we can linearize the total potential about the equilibrium positions. The resulting harmonic oscillations constitute normal modes of the ion crystal. Solving the relevant eigenvalue equation gives the normal mode frequencies $\omega_z \xi_k$ and eigenvectors $\vec{v}^{(k)}$ of the N normal modes. For two and four ions the normal mode eigenvectors and eigenvalues are given in table 2. For any number of ions, the lowest-frequency mode is always the centre-of-mass (COM) mode, in which the ion string moves as a unit, with no relative motion between the ions. The Coulomb interaction then has no effect on the dynamics of the COM mode, so the COM frequency is just equal to the single-ion trap frequency ω_z . Because of the symmetry of the ion string about $z = 0$, the ions' relative amplitudes of motion in a given mode are either symmetric or antisymmetric about the centre of the string, as seen in table 2.

It is easy to quantize the normal modes, since each mode is just a simple harmonic oscillator. We consider only the axial modes for simplicity. Writing the operator for small

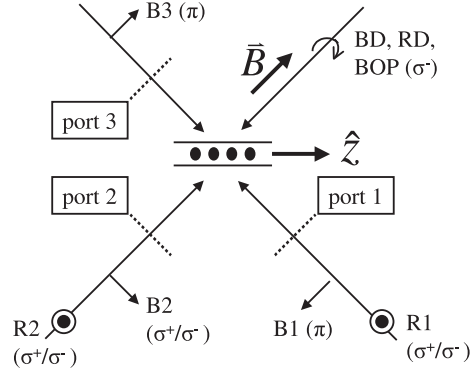


Figure 3. Beam geometry for our experiments. Initialization and detection beams are labelled ‘BD’ (blue Doppler) and ‘RD’ (red Doppler). Raman beams are labelled by frequency as B (the bluer beam) or R (the redder beam) and by the port at which they enter as 1, 2 or 3. Thus the bluer beam entering port 1 is denoted B1. Polarizations are specified in the atomic basis $\{\sigma^+, \sigma^-, \pi\}$ selected by the quantization field. The trap defines the spatial coordinate system, with the trap axis along \hat{z} .

displacements of the i th ion as \mathbf{x}_i and the conjugate momentum as \mathbf{p}_i , we define the annihilation operator \mathbf{a}_k for the k th mode in the usual way:

$$\mathbf{a}_k = \sqrt{\frac{Nm\xi_k\omega_z}{2\hbar}} \sum_{i=1}^N v_k^{(i)} \left(\mathbf{x}_i + \frac{i}{Nm\xi_k\omega_z} \mathbf{p}_i \right). \quad (1)$$

3. Initialization and readout

Quantum computation requires the preparation of the computational register in a well-defined input state at the beginning of the computation and the efficient readout of the state of the register at the end of the computation. We chose the logic states to be two hyperfine sublevels of the ${}^9\text{Be}^+$ ion, namely $|\downarrow\rangle = |F = 2, m_F = -2\rangle$ and $|\uparrow\rangle = |F = 1, m_F = -1\rangle$. All the experiments described here began by initializing the ions to the $|\downarrow\rangle$ logic state and ended by detecting the number of ions in the $|\downarrow\rangle$ state. These tasks were accomplished by two laser beams, called ‘blue Doppler’ (BD) and ‘red Doppler’ (RD), which were nearly resonant with the ${}^2S_{1/2} |F = 2\rangle \leftrightarrow {}^2P_{3/2}$ and ${}^2S_{1/2} |F = 1\rangle \leftrightarrow {}^2P_{1/2}$ atomic transitions, respectively. The Zeeman splitting of the magnetic sublevels was about 24 MHz, comparable to the 19.4 MHz excited-state linewidth. Both beams propagated along the quantization axis \vec{B} and were polarized σ^- , as shown in figure 3. At the beginning of each shot of an experiment, we applied the BD and RD beams at the same time for about 20 μs , then left RD on for an additional few μs . This procedure optically pumped the ions into the $|\downarrow\rangle$ state with a probability exceeding 99.9%. The extra few μs of RD ensured that the ions would not be pumped into a dark hyperfine superposition [20] in the event of imperfect BD or RD polarization. BD was always detuned from the exact $|\downarrow\rangle \leftrightarrow {}^2P_{3/2}$ resonance by 8 MHz to ensure that the ions were cooled to the Doppler cooling limit at the beginning of each shot.

We detected the number of ions in $|\downarrow\rangle$ by turning on BD for several hundred microseconds and detecting the scattered light on either a multichannel plate imager (MCP) or a photomultiplier tube (PMT). Assuming perfect σ^-

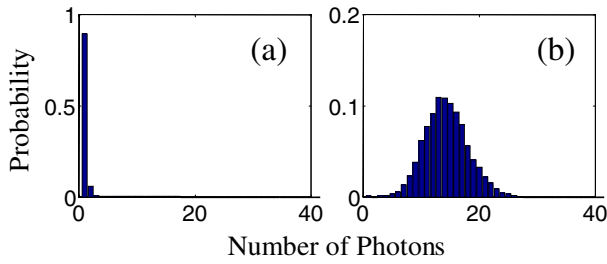


Figure 4. Histograms of the number of photons detected from a single ion over 1000 shots of the experiment. The ion was illuminated by BD alone for $200 \mu\text{s}$. (a) Ion prepared in $|\uparrow\rangle$ for each shot. (b) Ion prepared in $|\downarrow\rangle$ for each shot.

polarization, an ion in $|\downarrow\rangle$ can make transitions only to the $|F = 3, m_F = -3\rangle$ hyperfine sublevel of the ${}^2P_{3/2}$ state. Dipole selection rules then force it to decay back to the $|F = 2, m_F = -2\rangle$ hyperfine sublevel, i.e. the $|\downarrow\rangle$ state. The number of photons scattered by a $|\downarrow\rangle$ ion on this cycling transition is limited only by the polarization of the BD beam, since pumping to other states can occur only for imperfect polarization. Since the linewidth of the ${}^2S_{1/2} \leftrightarrow {}^2P_{3/2}$ transition is 19.4 MHz and the hyperfine splitting is 1.25 GHz, the states $|\uparrow\rangle$ and $|\downarrow\rangle$ are spectrally well resolved. Thus we could illuminate the ion with BD for hundreds of microseconds, scattering many photons if the ion is in $|\downarrow\rangle$, but scattering very few if the ion is in $|\uparrow\rangle$. The detection duration is limited by off-resonant repumping of $|\uparrow\rangle$ to $|\downarrow\rangle$ by BD, which eventually causes an initially dark ion to scatter many photons. This technique for high-efficiency internal state discrimination is commonly used in studies of trapped ions [21–23].

By performing many repetitions, or shots, of an experiment and binning the results according to the number of photons detected, we could build up a histogram of the photon statistics for that experiment. Figure 4 shows such a histogram for an ion prepared in $|\uparrow\rangle$, and another histogram for an ion prepared in $|\downarrow\rangle$. The two histograms are readily distinguished. The $|\downarrow\rangle$ histogram is Poissonian, but off-resonant repumping of the $|\uparrow\rangle$ state to $|\downarrow\rangle$ causes the $|\uparrow\rangle$ histogram to deviate from a Poissonian distribution, increasing the overlap between the two histograms [24].

In experiments with one ion, we might detect the ion in $|\downarrow\rangle$ on some shots and in $|\uparrow\rangle$ on others, for instance if we prepared the ion in a superposition state. An example histogram showing this situation is shown in figure 5. We fit such histograms to a weighted sum of two reference histograms like those shown in figure 4. In each shot of the experiment, the ion was projected into either the state $|\downarrow\rangle$ or the state $|\uparrow\rangle$, in accordance with the quantum measurement postulate, so fitting the histogram was similar to counting up the number of times that the ion was projected into $|\downarrow\rangle$ or $|\uparrow\rangle$ over the course of many experiments. On the other hand, if we wanted to read out the ion state on a shot-by-shot basis, we could set a discriminator at, say, four photons detected (for the case of figure 4). Then we considered the ion to be in state $|\downarrow\rangle$ if more than four photons were detected for a particular shot. The discriminator method was conceptually simpler but yielded lower signal-to-noise for the measurement of $|\downarrow\rangle$ and $|\uparrow\rangle$ probabilities than the histogram method, because it did not take into account the details of the count distributions in the overlap region between

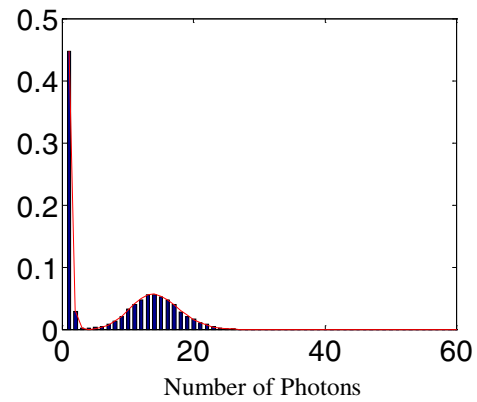


Figure 5. Histogram of the number of photons detected from a single ion prepared in a superposition of $|\downarrow\rangle$ and $|\uparrow\rangle$ over 1000 shots. The solid line is the best fit to the theoretical count distribution.

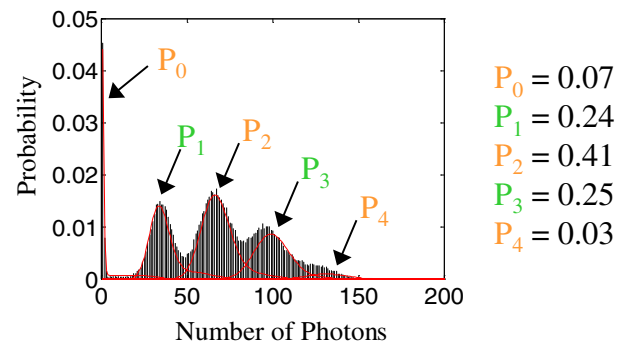


Figure 6. Histogram for four ions prepared in a superposition state. The solid line shows the best fit to a sum of reference histograms.

the $|\downarrow\rangle$ and $|\uparrow\rangle$ reference histograms. However, even using the discriminator method, the small overlap of the reference histograms permitted routine detection efficiencies of 98% in a single shot.

In experiments with multiple ions, we collected all the fluorescence from the ion string at once, making no attempt to spatially resolve the ions. Thus we detected only the number of ions in $|\downarrow\rangle$, rather than reading out the ions individually. Typically we collected histograms of photon count distribution as a function of an experimental parameter. In these cases we constructed reference histograms by fitting weighted sums of theoretical photon count distributions for zero, one, \dots ions in state $|\downarrow\rangle$ to a histogram created by averaging all the data histograms [24]. The free parameters in the theoretical distributions were the mean number of photons collected per ion in $|\downarrow\rangle$ and the mean number of photons due to background light. The effect of off-resonant repumping was included for each reference histogram. Optical pumping due to imperfect BD polarization was not included in the fits. The weights in the fits to the data histograms then gave the probabilities P_0, P_1, \dots of finding zero ions in $|\downarrow\rangle$, one ion in $|\downarrow\rangle$ etc. An example histogram for four ions, including a fit to reference histograms, is shown in figure 6. Histograms built up over 1000 shots yielded probabilities P_i with typical uncertainties of ± 0.01 for two ions and ± 0.02 for four ions. It is also possible to use the discriminator method for multiple ions, but the signal-to-noise is relatively low unless a more elaborate readout scheme is used (see below).

4. Coherent coupling of logic states

We used two-photon stimulated Raman transitions to coherently manipulate the ion internal and motional states. The laser beams driving the transitions were typically detuned by $\Delta \sim 2\pi \times 100$ GHz from the nearest $S \leftrightarrow P$ resonance, so we can adiabatically eliminate the excited state. It is then convenient to consider the $|\downarrow\rangle, |\uparrow\rangle$ states as forming a spin- $\frac{1}{2}$ system with spin operator \vec{S} . We write ω_1 and ω_2 for the angular frequencies of the two beams, Ω_1 and Ω_2 for their one-photon resonant Rabi frequencies, \vec{k}_1 and \vec{k}_2 for their wavevectors and φ_1 and φ_2 for their phases at the position of the ion in question. For a two-photon detuning $\delta = \omega_1 - \omega_2$, which we typically set close to the energy splitting $\omega_{\downarrow\uparrow}$ between $|\uparrow\rangle$ and $|\downarrow\rangle$, we find the Raman Hamiltonian [24–26]

$$\mathbf{H}_{\text{Raman}} = -\delta S_z + \Omega_R [e^{i\phi} e^{i\vec{\Delta}\vec{k}\cdot\mathbf{x}} \mathbf{S}_+ + \text{h.c.}] \quad (2)$$

where the ‘Raman phase’ $\phi = \varphi_1 - \varphi_2$ and the Raman Rabi frequency $\Omega_R \equiv 2\Omega_1\Omega_2/\Delta$. Evidently the motional dynamics depend only on $\vec{\Delta}\vec{k}$. The apparently insignificant quantity ϕ is one of the most important parameters in our experiments, as we will see.

For copropagating Raman beams, e.g. B1 and R1 in figure 3, and on two-photon resonance $\delta = \omega_{\downarrow\uparrow}$, the Hamiltonian (2) induces Rabi flopping between $|\downarrow\rangle$ and $|\uparrow\rangle$ according to

$$\begin{pmatrix} C_{\downarrow}(t) \\ C_{\uparrow}(t) \end{pmatrix} = \begin{pmatrix} \cos \Omega_R t & -ie^{i\phi} \sin \Omega_R t \\ -ie^{-i\phi} \sin \Omega_R t & \cos \Omega_R t \end{pmatrix} \begin{pmatrix} C_{\downarrow}(0) \\ C_{\uparrow}(0) \end{pmatrix} \quad (3)$$

where the atomic wavefunction $\Psi = C_{\downarrow}(t)|\downarrow\rangle + C_{\uparrow}(t)|\uparrow\rangle$. We used this ‘copropagating carrier’ evolution mainly as a diagnostic tool in the experiment, since it enabled us to prepare arbitrary single-ion qubit states in a way that did not depend on the ion motional state.

Entangling the ions, on the other hand, required coupling of the ion spins to a shared motional mode. We performed almost all our quantum logic operations using Raman beams B1 and R2 (see figure 3) with an angular separation of 90° and with $\vec{\Delta}\vec{k}$ parallel to the trap axis \hat{z} . For this beam geometry, the Raman transitions depend on the ion motion along the trap axis, but not along the other two axes. This fact simplifies the dynamics enormously: for N ions we need only consider the N axial normal modes rather than the full set of $3N$ motional modes. In the experimental situation, the ions were in the Lamb–Dicke limit, for which the ion wavepacket is much smaller than the wavelength of the Raman beam interference pattern. In particular, the parameter $\eta \equiv \sqrt{2}kz_0$ is small, where $z_0 = \sqrt{\hbar/(2m_{\text{ion}}\omega_z)}$ is the zero-point wavepacket spread along \hat{z} . Since $\omega_{\downarrow\uparrow}$ is small compared to the $S \leftrightarrow P$ transition frequency, we have $k \equiv |\vec{k}_1| \approx |\vec{k}_2|$. For a single ion, we find three two-photon resonances, the ‘carrier’ at $\delta = \omega_{\downarrow\uparrow}$ and the ‘blue’ and ‘red’ sidebands at $\delta = \omega_{\downarrow\uparrow} \pm \omega_z$. The corresponding Hamiltonians are

$$\mathbf{H} = \Omega_R e^{i\phi} \mathbf{S}_+ + \text{h.c.} \quad \delta = \omega_{\downarrow\uparrow} \quad (4)$$

$$= \eta \Omega_R e^{i\phi} \mathbf{S}_+ \mathbf{a} + \text{h.c.} \quad \delta = \omega_{\downarrow\uparrow} - \omega_z \quad (5)$$

$$= \eta \Omega_R e^{i\phi} \mathbf{S}_+ \mathbf{a}^\dagger + \text{h.c.} \quad \delta = \omega_{\downarrow\uparrow} + \omega_z \quad (6)$$

where \mathbf{a} is the annihilation operator for the quantized motion along \hat{z} and $\mathbf{S}_+ = |\uparrow\rangle\langle\downarrow|$. The resonances are well resolved in

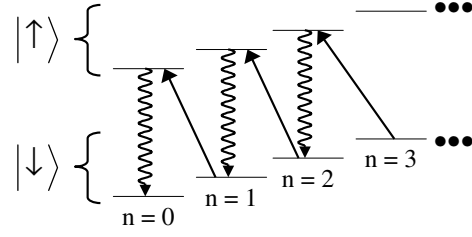


Figure 7. Raman cooling of the motion of a single trapped ion. A series of pulses on the red sideband moves the population of the motional state $|K\rangle$ to $|K-1\rangle$, then moves $|K-1\rangle$ to $|K-2\rangle$ etc, until all the population resides in $|0\rangle$.

the experiment, so near a sideband resonance the ion undergoes Rabi flopping between $|\downarrow, n\rangle$ and $|\uparrow, n \pm 1\rangle$ with the Rabi frequency $\Omega_{\text{sb}} = \eta\Omega_R$. For multiple ions, one observes a pair of red and blue sidebands for each normal mode of motion along \hat{z} with similar Rabi flopping dynamics, except that \vec{S} is replaced by the collective spin operator $\vec{J} = \sum_j \vec{S}_j$.

5. Cooling the ion motion

At the end of each shot of an experiment, we applied BD for several hundred microseconds, cooling the ions to the Doppler limit (about 10 MHz of energy). To reduce errors in our quantum logic operations, we used resolved-sideband Raman cooling [3, 27, 28] to cool the ions further. For clarity, we first consider Raman cooling on a single motional mode of a single ion. Suppose the ion is initially in $|\downarrow; n=1\rangle$. A pulse of appropriate duration applied to the red sideband drives this state to $|\uparrow; n=0\rangle$. Then, optically pumping to the state $|\downarrow; n=0\rangle$, we see that the motional mode has been cooled by one phonon [28]. Because the ion is in the Lamb–Dicke limit, the optical pumping is nearly recoilless and is unlikely to heat the ion [29, 30].

In practice, the ions start in a thermal state, so the distribution of phonon number states is broad. Given a small probability of occupying states with more than K phonons, we could cool the whole distribution to the ground state by applying K cycles of Raman drive and optical pumping so that the first Raman pulse transfers all the population in $|K\rangle$ to $|K-1\rangle$, the second pulse transfers $|K-1\rangle$ to $|K-2\rangle$ etc. This process is shown in figure 7. The Raman and optical pumping pulses typically lasted a few microseconds each.

We could not use BD in repumping the ions to $|\downarrow\rangle$. While photon scattering is nearly recoilless in the Lamb–Dicke limit, the hundreds or thousands of photons scattered on the cycling transition would certainly cause the ion to equilibrate to the Doppler cooling limit [27]. Rather, we needed to optically pump to $|\downarrow\rangle$ while scattering only a few photons. Scattering a few RD photons ensures that the ion resides in the ${}^2S_{1/2} |F=2\rangle$ manifold, but does not select the $m_F = -2$ magnetic state. To pump to $m_F = -2$, we applied RD and the blue optical pumping (BOP) beam simultaneously. BOP is polarized σ^- in the atomic basis and is tuned to the ${}^2S_{1/2} |F=2\rangle \leftrightarrow {}^2P_{1/2} |F=2\rangle$ transition. (BD is instead tuned to the ${}^2P_{3/2}$ transition.) Dipole selection rules kept $|\downarrow\rangle$ dark to BOP, while all other ${}^2S_{1/2} |F=2\rangle$ transitions were bright to BOP. Hence the cycling transition was never excited

by BOP and the ion only scattered a few photons before arriving at the dark $|\downarrow\rangle$ state. The few photons scattered from BOP and RD caused almost no heating of the ion during the optical pumping step.

To cool multiple motional modes of an ion crystal, we applied several Raman cooling cycles to each mode in succession. In this case, however, it was quite difficult to find the appropriate Raman pulse durations corresponding to the procedure above, since we were coupling a single motional mode to several spins simultaneously. Experimental data and a theoretical treatment for the two-ion case can be found in [4]. We could cool the stretch modes to the ground state almost perfectly, but because of the heating of the COM mode [31] usually about one phonon remained in the COM mode. The precise cooling limit depended on the number of ions and the trap frequency. The remaining motion in the COM mode impacted the fidelity of our entangling gate for four atoms.

6. Multiparticle entanglement

So far we have described initialization of our quantum register, operations on single qubits and detection of the register state. However, one more ingredient is needed to perform quantum computation over the whole Hilbert space: a logic gate that entangles two particles [32–34]. This gate is a unitary evolution that takes an initially separable state to an entangled state, and can be a quantum XOR [11, 35], a phase gate [25, 36, 37], or any of a class of equivalent gates. We implemented the entangling gate of Mølmer and Sørensen [38, 39] for strings of two and four ions [10], realizing the operations

$$|\downarrow\downarrow\rangle \rightarrow |\downarrow\downarrow\rangle + |\uparrow\uparrow\rangle \quad |\downarrow\downarrow\downarrow\downarrow\rangle \rightarrow |\downarrow\downarrow\downarrow\downarrow\rangle + |\uparrow\uparrow\uparrow\uparrow\rangle. \quad (7)$$

One can use this gate on two ions in conjunction with single-qubit operations to construct an XOR gate [38], so this gate enables universal quantum logic. Of course, our experiment only approximates the evolution (7). However, measurements on the states produced in the experiment showed that those states were, in fact, entangled. We used the two-ion version of this gate as our fundamental entangling gate in the experiments described below.

To apply the Mølmer–Sørensen entangling gate to an ion crystal, one off-resonantly drives both the red and blue sidebands of a particular motional mode of the crystal. The two-photon detunings Δ_M from the sidebands are equal and opposite. Each ion is coupled to each sideband with the same Rabi frequency $\Omega_{sb} \sim \eta\Omega_R$. The relevant level scheme for two ions is shown in figure 8. We obtain the coupling condition by keeping the intensity of all Raman beams constant across the ion crystal and by choosing a motional mode in which all ions have equal motional amplitudes, i.e., $|v_i^{(k)}|$ is independent of the ion index i .

The essential features of the entangling gate are intuitively clear in the far-detuned limit $\Delta_M \gg \Omega_{sb}$. Considering only two ions for clarity, we see that the intermediate spin state $|\downarrow\uparrow\rangle + |\uparrow\downarrow\rangle$ is only virtually populated, while the $|\downarrow\downarrow\rangle \leftrightarrow |\uparrow\uparrow\rangle$ transition is resonant. The singlet spin state $|\downarrow\uparrow\rangle - |\uparrow\downarrow\rangle$ is invariant under \vec{J} , so it does not take part in the dynamics. The situation is reminiscent of resonant two-photon excitation through a virtual intermediate level [40], as

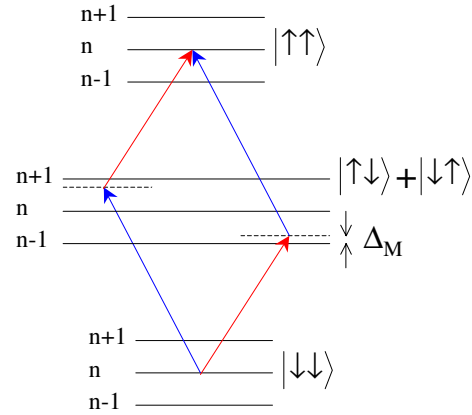


Figure 8. Relevant level scheme for the two-ion version of the entangling gate. The arrows represent Raman processes driven by pairs of Raman beams. The two pathways through the intermediate $|\downarrow\uparrow\rangle + |\uparrow\downarrow\rangle$ state exhibit quantum interference.

in, e.g., spectroscopy of the rubidium $5S \leftrightarrow 5D$ transition. However, the ‘two-photon resonance’ here corresponds to simultaneous excitation of two ions, rather than excitation of a high-lying level of a single atom, and the off-resonant ‘single-photon’ couplings are actually Raman processes. Exploiting the analogy to two-photon spectroscopy, we see that the Rabi frequency for the pathway through the intermediate $|n+1\rangle$ (respectively $|n-1\rangle$) state is proportional to $(n+1)\Omega_{sb}^2/\Delta_M$ (respectively $n\Omega_{sb}^2/\Delta_M$) in the Lamb–Dicke limit. The factors of n come from the harmonic oscillator raising and lowering operators. The two paths interfere destructively, so the overall Rabi frequency for the $|\downarrow\downarrow\rangle \leftrightarrow |\uparrow\uparrow\rangle$ transition is proportional to Ω_{sb}^2/Δ_M . In the Lamb–Dicke limit, the Rabi frequency is independent of n , so the gate is insensitive to the initial motional state of the ion crystal! Because of the heating in our traps, this feature gave the Mølmer–Sørensen gate a distinct advantage over the Cirac–Zoller XOR [35], which requires that the ion crystal start in a motional number state.

It takes a relatively long time ($\gg 1/\Omega_{sb}$) to apply the entangling gate in the far-detuned limit, giving decoherence a long time to act and severely limiting the gate fidelity. However, one can obtain the evolution (equation (7)) even if Δ_M is on the order of Ω_{sb} , for carefully chosen values of Δ_M [41]. In the experiment we used this ‘nonperturbative’ gate operation to speed up the gate to times of order $1/\Omega_{sb}$, allowing high-fidelity gate operation. Furthermore, we had to select a motional mode for logic that coupled equally to the ions. The obvious choice was the COM mode in each case, but because of the large heating rate of the COM mode, we selected higher-order modes in both cases. For the two-ion experiments we used the (axial) stretch mode with frequency $\sqrt{3}\omega_z$, while for four ions we used the (axial) stretch 2 mode with frequency $\approx\sqrt{29/5}\omega_z$ (see table 2). In general, the only mode with equal coupling is the COM mode, so the equal coupling of the stretch 2 mode of four ions was a lucky coincidence for us. To ensure equal illumination of each ion, we used beam spot sizes at least twice as large as the extent of the ion crystal.

The entangling gate required coupling on two Raman transitions. Rather than using two pairs of Raman beams to generate the two Raman difference frequencies, we modulated R2 using a resonant EOM. The R2 carrier frequency ω_{R2} beat

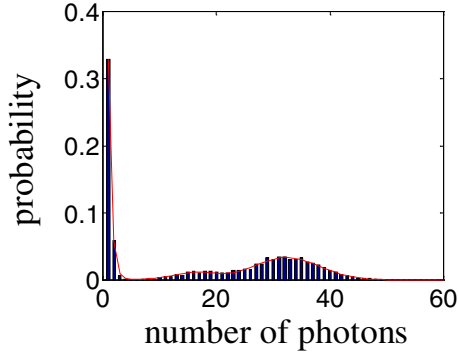


Figure 9. Histogram of photon counts obtained after application of the entangling gate to two ions.

with the B1 frequency ω_{B1} to give a beatnote near the blue sideband, while one of the EOM-generated sidebands of R2 beat with B1 to give a beatnote near the red sideband. To provide equal coupling to each sideband, we set the EOM power so that the intensities of the EOM sidebands were equal to the intensity of the (depleted) R2 carrier. In this set-up, only the EOM carrier and one EOM sideband were useful for driving the entangling gate.

The spin population of the states produced by the evolution (7) is nominally equally divided between $|\downarrow^N\rangle$ and $|\uparrow^N\rangle$ for N ions. Figure 9 shows a histogram of count rates obtained after application of the entangling gate. As expected, the histogram shows a bimodal distribution of count rate. Fitting the populations for this histogram gave probabilities $P_0 = 0.43$, $P_1 = 0.11$ and $P_2 = 0.46$, where P_n is the probability of finding n ions in $|\downarrow\rangle$. The error in each value is ± 0.01 . The populations are quite close to the ideal case $P_0 = 0.50$, $P_1 = 0.00$ and $P_2 = 0.50$. For four ions we typically found $P_0 \approx 0.35$, $P_1 \approx P_2 \approx P_3 \approx 0.10$ and $P_4 \approx 0.35$. This distribution implies that a large fraction of the population resides outside the desired state. However, there are 14 orthogonal states that give one, two or three ions in $|\downarrow\rangle$, and only two orthogonal states in the desired entangled state, so the distribution of population over the 16 orthogonal states is far from random.

Ideally, the evolution (7) produces full coherence between the $|\downarrow^N\rangle$ and $|\uparrow^N\rangle$ states, so that $|\rho_{\downarrow^N, \uparrow^N}| = 0.5$. To measure the coherence produced in the experiment, we ‘interfered’ the $|\downarrow^N\rangle$ and $|\uparrow^N\rangle$ states using a variant of the method proposed in [42]. After the entangling gate, we applied a carrier $\pi/2$ pulse on all ions with a variable RF phase. We then detected the number N_\downarrow of ions in $|\downarrow\rangle$ and computed the parity $\Pi(\phi) \equiv (-1)^{N_\downarrow}$. Assuming an ideal carrier pulse, we have

$$\Pi(\phi) = 2|\rho_{\downarrow^N, \uparrow^N}| \cos N\phi \quad (8)$$

so we could extract the desired coherence by measuring the parity as a function of phase. To obtain the interference data, we took histograms of the photon counts at each value of the phase ϕ over several oscillations of the sinusoid equation (8). Averaging all the histograms together and fitting the result determined the mean count number per ion and the mean number of background counts. From this information we constructed reference histograms for $N_\downarrow = 0, 1, \dots, N$. Fitting the individual histograms to the references gave the

probabilities $P_n(\phi)$ of finding $N_\downarrow = n$ at phase ϕ , from which we could trivially infer $\Pi(\phi)$. Figure 10 shows results of interference experiments for two and four ions. Each curve is fitted with a single sinusoid with frequency fixed by equation (8) to obtain the amplitude. The presence of other oscillation frequencies in the interference data would imply coherences involving fewer than N ions. Since the fits to the data are good, we infer that $\rho_{\downarrow^N, \uparrow^N}$ is by far the largest off-diagonal element of the density matrix in each case. In principle, other coherences could be present, but the interference data would constrain these coherences to have particular phase relationships that seem physically unlikely. The data of figure 10 show $|\rho_{\downarrow^N, \uparrow^N}| = 0.39 \pm 0.01$ for two ions and 0.22 ± 0.02 for four ions.

We can easily establish the separability or entanglement of the experimental density matrix ρ by computing its fidelity $F = \langle \psi_{\text{ent}} | \rho | \psi_{\text{ent}} \rangle$ against the ideal state $\psi_{\text{ent}} = (|\downarrow^N\rangle + |\uparrow^N\rangle)/\sqrt{2}$. Any factorizable density matrix satisfies $F = \langle \psi_{\text{ent}} | \rho | \psi_{\text{ent}} \rangle \leq 1/2$ [10]. This condition is sufficient but not necessary to show entanglement [43]. By measuring the populations $\rho_{\downarrow^N, \downarrow^N}$, $\rho_{\uparrow^N, \uparrow^N}$ and the coherence $|\rho_{\downarrow^N, \uparrow^N}|$, we established [10]

$$F = 0.83 \pm 0.01 \quad N = 2 \quad (9)$$

$$F = 0.57 \pm 0.02 \quad N = 4 \quad (10)$$

showing that the entangling gate can indeed produce entangled states of two and four ions.

For the two-qubit state, we can approximate the entanglement of formation from the measured density matrix elements as $E \approx 0.5$ [44]. This quantity measures the increase in the entropy of one qubit produced by tracing over the other qubit. Ideally, tracing over one qubit leaves the other in a mixture of half $|\downarrow\rangle$ and half $|\uparrow\rangle$, with no coherence remaining between $|\downarrow\rangle$ and $|\uparrow\rangle$. In this case $E = 1$. The entanglement of formation also gives an upper bound on the entanglement of distillation E_D [45, 46]. Leaving out the technical details, any procedure designed to distill a perfect EPR state $|\downarrow\uparrow\rangle - |\uparrow\downarrow\rangle$ from several copies of a partially entangled two-qubit state requires an average of $1/E_D$ copies [47]. The complexity of the quantum communications tasks is often quantified in terms of the number of EPR states required, so E_D measures the usefulness of the experimental state ρ . We see that of the order of two copies of our two-qubit state ρ are required to distill one EPR state.

There is so far no simple way to characterize the amount of entanglement of a general four-qubit state. However, the absence of coherences other than $\rho_{\downarrow^4, \uparrow^4}$ in the interference data suggests that we can write the experimental four-ion density matrix as a sum of the desired entangled state and a state with no coherences at all. In this decomposition we find [10]

$$\rho \approx 0.43|\psi_{\text{ent}}\rangle\langle\psi_{\text{ent}}| + 0.57\rho_{\text{diag}} \quad (11)$$

where ρ_{diag} has no off-diagonal elements. Thus, not only is the total density matrix entangled, but any one shot of the experiment has a significant chance of producing the desired state.

In the following, we describe the quantum logic operations in terms of entangling gates and carrier evolutions. The

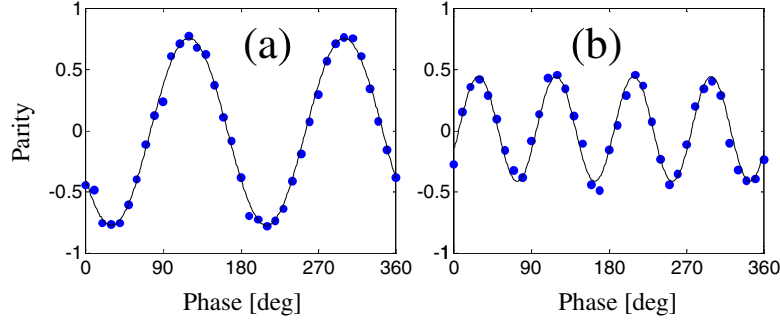


Figure 10. Interference data for (a) two and (b) four ions. Dots are data points; solid curves are sinusoidal fits with frequencies fixed by equation (8). The fit amplitudes show $|\rho_{\downarrow N, \uparrow N}| = 0.39 \pm 0.01$ for two ions and 0.22 ± 0.02 for four ions.

entangling gate operates on an arbitrary state as

$$U_{\text{ent}}(\phi_1, \phi_2) = \exp[i\pi J_y^2/2] \quad (12)$$

$$\rightarrow \frac{1+i}{2} [\mathbf{1} - i(e^{i(\phi_1+\phi_2)}|\uparrow\uparrow\rangle\langle\downarrow\downarrow| + e^{-i(\phi_1+\phi_2)}|\downarrow\downarrow\rangle\langle\uparrow\uparrow|) \quad (13)$$

$$\times (\langle\uparrow\uparrow| - e^{i(\phi_1-\phi_2)}|\uparrow\downarrow\rangle\langle\downarrow\uparrow| - e^{-i(\phi_1-\phi_2)}|\downarrow\uparrow\rangle\langle\uparrow\downarrow|)] \quad (14)$$

for ϕ_1 and ϕ_2 the Raman phases at the two ions. The normalized carrier evolution acts as

$$U_{\text{car}}(\theta, \phi_1, \phi_2) = \bigotimes_{j=1,2} \left[\mathbf{1} \cdot \cos \frac{\theta}{2} - i \sin \frac{\theta}{2} (e^{i\phi_j} |\uparrow\rangle\langle\downarrow| + e^{-i\phi_j} |\downarrow\rangle\langle\uparrow|) \right] \quad (15)$$

for a carrier drive of duration $t = \theta/\Omega_R$. As shown below, we could control ϕ_1 and ϕ_2 independently for two ions.

7. Violation of a Bell inequality

Perhaps the most striking feature of quantum mechanics is its denial of local realism. The uncertainty principle requires us to believe that measuring the position of an object can change its momentum, but is still consistent with the basic notion of realism: that the object had some position or other before the measurement, which is then perturbed by the act of measurement. At the same time, special relativity insists on locality: the measured position does not depend on events outside the lightcone of the object. As shown by Einstein *et al* [48], quantum mechanics is incomplete if we assume local realism. Bell [49] proved that quantum mechanics is actually inconsistent with local realism, deriving an inequality on observables that is satisfied by all local realistic theories but is violated by quantum mechanics. Many experiments [50–55] have observed violation of a Bell inequality, so that local realistic theories are now discounted by the vast majority of physicists. The result of this reasoning is epistemologically remarkable. One must either accept that ‘objective reality’ is created only at the moment of measurement, or give up special relativity! Mainstream physics has opted to retain special relativity, probably a good choice in view of the massive experimental evidence in favour of quantum field theory. Moreover, the philosophical tradition of Mach and, later, Heisenberg and Bohr, restricts the domain of physics to properties susceptible to measurement, so one can dispense with realism in a Machian theory. The alternative view of Bohm [56, 57] retains realism at the expense of locality,

introducing a ‘pilot-wave’ field that coordinates the behaviour of particles at widely separated points.

Clausner, Horne, Shimony and Holt (CHSH) [58] proposed an experimental arrangement to test a form of Bell’s inequality quantitatively. Here a ‘black box’ prepares a pair of particles. The i th particle ($i = 1, 2$) enters a measurement apparatus whose properties are parametrized by an independent classical variable Φ_i . Each (classical) measurement yields a value $M_i(\Phi_i) = \pm 1$ depending on the parameter Φ_i and the state of the correlated particles. Averaging over many measurements, one extracts the correlation function $q(\Phi_1, \Phi_2) = \langle M_1(\Phi_1)M_2(\Phi_2) \rangle$. Then the CHSH form of the Bell inequality

$$B(a_1, d_1, b_2, c_2) \equiv |q(d_1, c_2) - q(a_1, c_2)| + |q(d_1, b_2) + q(a_1, b_2)| \leq 2 \quad (16)$$

holds for any values a_1, d_1 (respectively b_2, c_2) of Φ_1 (respectively Φ_2) under the assumption of local realism [58]. The derivation of equation (16) involves the quantity $\langle M_1(a_1)M_1(d_1)M_2(b_2)M_2(c_2) \rangle$. Since the terms $M_1(a_1), M_1(d_1)$ refer to different arrangements of the experiment for $a_1 \neq d_1$, quantum mechanics forbids us to speak of both terms at once. Hence the product $M_1(a_1)M_1(d_1)$ is not well defined in quantum mechanics, allowing violation of equation (16).

In our experiment, the entangling gate played the role of the CHSH ‘black box’, preparing two ions in the state $|\downarrow\downarrow\rangle + |\uparrow\uparrow\rangle$. To measure the ion correlation function $q(\phi_1, \phi_2)$, we applied a carrier rotation $U_{\text{car}}(\theta = \pi/2, \phi_1, \phi_2)$ and built up a histogram of photon counts. Counting the number of events N_0 (N_1, N_2) with zero (one, two) ions bright, we find

$$q(\Phi_1, \Phi_2) = \frac{(N_0 + N_2) - N_1}{N_{\text{tot}}}. \quad (17)$$

To measure $B(a_1, d_1, b_2, c_2)$, we obtained a value of q for each term in equation (16). We chose a_1 , etc, so as to give the maximum violation of equation (16) by the quantum mechanical prediction for B , which occurs for

$$\begin{aligned} a_1 &= -\pi/8 & d_1 &= 3\pi/8 \\ b_2 &= -\pi/8 & c_2 &= 3\pi/8. \end{aligned} \quad (18)$$

For these angles we have the prediction $B = 2\sqrt{2}$, contradicting the bound (16) set by local realism.

Independently setting ϕ_1 and ϕ_2 for the carrier rotation required setting the Raman phases of the two ions

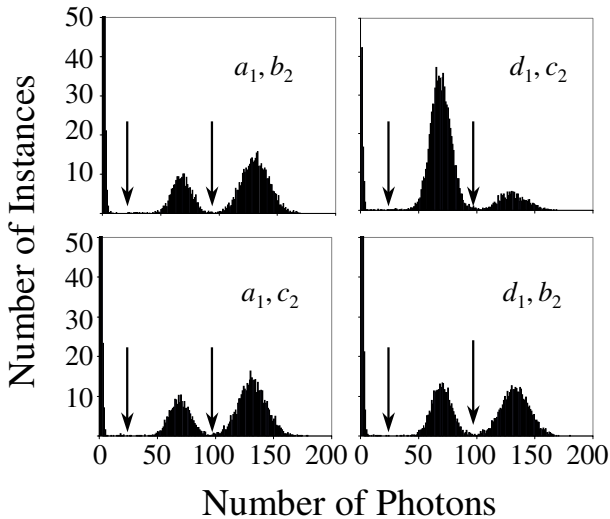


Figure 11. Histograms of fluorescence signals for the four sets of phases given in equation (18). The vertical arrows break up the data into cases of zero, one or two ions bright with 98% accuracy.

independently. Changing the phase of the RF driving the R2 double-pass AOM shifted the interference pattern between the Raman beams by a constant amount, allowing us to control the quantity $\phi_{\text{tot}} = \phi_1 + \phi_2$. However, the phase difference $\Delta\phi = \phi_1 - \phi_2$ is set by the separation of the ions Δz along \hat{z} as $\Delta\phi = \sqrt{2}k\Delta z$. To control $\Delta\phi$ without changing ϕ_{tot} , we varied the endcap voltage, and therefore the trap strength, so that the ions moved symmetrically about the centre of the trap. Hence the endcap voltage and the RF phase jointly determined the phases ϕ_1, ϕ_2 [6].

We repeated the experiment $N_{\text{tot}} = 20\,000$ times for each of the four sets of phases given by equation (18). These data are presented as histograms in figure 11. To determine the values N_0, N_1 and N_2 entering equation (17), we divided the histograms into cases of zero, one or two ions bright by setting discriminators at the positions of the arrows in figure 11. This procedure gives the same value of q that we would obtain by measuring M_1 and M_2 individually for each shot of the experiment.

We measured the Bell signal five times to estimate the variation between runs. The five sets of correlation functions and the resulting Bell signals are shown in table 3. The statistical error of each Bell signal was ± 0.01 . Averaging the Bell signals together, we find

$$B\left(-\frac{\pi}{8}, \frac{3\pi}{8}, -\frac{\pi}{8}, \frac{3\pi}{8}\right) = 2.25 \pm 0.03 \quad (19)$$

an 8σ violation of the Bell inequality (16).

The error in the average Bell signal significantly exceeds the statistical error predicted from table 3. We attributed this discrepancy to drifts of the RF phase, which induce errors in setting the angles a_1 , etc, for the four measurements of q , but these errors cannot be estimated from the statistical errors in q . The phase drift was usually constant for a few minutes at a time, but could change magnitude and direction rapidly and randomly. The drift sometimes amounted to several tens of mrad per minute, while about 15 min were required to make the four measurements of q needed for one measurement of B . Including the drift in the error analysis for each measurement

Table 3. The correlation values and resulting Bell signals for five runs of the experiment. The phase angles a_1, d_1, b_2 and c_2 are given by equation (18). The statistical errors are 0.006 and 0.012 for the values of q and B respectively.

$q(a_1, b_2)$	$q(a_1, c_2)$	$q(d_1, b_2)$	$q(d_1, c_2)$	$B(a_1, d_1, b_2, c_2)$
0.541	0.539	0.569	-0.573	2.222
0.575	0.570	0.530	-0.600	2.275
0.551	0.634	0.590	-0.487	2.262
0.575	0.561	0.559	-0.551	2.246
0.541	0.596	0.537	-0.571	2.245

of B approximately accounts for the statistical error in the average value of B .

All previous experiments showing violation of Bell's inequality had quite low detector efficiencies, so that the number of particle pairs produced by the 'black box' far exceeded the number of events used for calculating the correlation function. To interpret these experiments as ruling out local realism, one assumes that the correlated pairs that are not detected exhibit the same behaviour as those that are detected, the fair sampling hypothesis. However, by violating this assumption it is possible to construct local realistic theories that reproduce the experimental data for detector efficiencies below a critical value, the so-called detection loophole [59, 60]. In these theories, the full set of particle pairs satisfies Bell's inequality, but the subset of pairs that is actually detected appears to violate it. While such a conspiracy of detectors seems quite unlikely, no previous experiment has been able to rule it out.

The experiment described here was the first to demonstrate a violation of Bell's inequality without use of the fair sampling hypothesis. Because we could prepare the entangled state on demand, we could make a measurement on every correlated pair. Thus there was no sampling involved in our experiment at all. In this situation, quantum mechanics predicts that uncorrelated errors in measuring the two particles simply lower the value of B . We estimate that we would have observed $B = 2.37$ in the absence of detection errors.

To falsify local realism using Bell's inequality, one must ensure that the only correlations between $M_1(\Phi_1)$ and $M_2(\Phi_2)$ arise from the correlations of the entangled pair. However, if the measuring devices can communicate during the measurement, i.e., if the measurement processes lie within each others' lightcones, we can attribute any violation of Bell's inequality to a conspiracy between the measuring devices rather than to any violation of local realism by the entangled particles. Tests of Bell's inequality using photons have gone to great lengths to close this 'locality loophole' [53–55]. In our experiment we could not ensure nonlocality because of the small separation between the ions. However, there is no physical reason to believe that the measurement outcomes influence each other in this way. We estimated the size of correlations arising from a wide variety of effects, including dipole–dipole interactions between the ions, interference between the radiation patterns of the ions and so on [61, 62]. In all cases the spurious correlations are negligible, but strictly speaking we have not closed the locality loophole. Similarly, the photon experiments [53–55] do not close the detection loophole, though there is no physical reason to believe in a

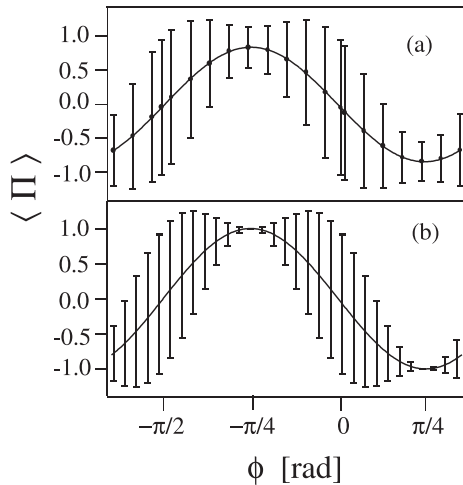


Figure 12. Mean and variance of the parity operator Π in the parity scheme for SSN interferometry. (a) Experimental data, 10 000 shots per point. Points give the mean value of Π as a function of ϕ ; error bars give the variance. The curve is the best fit to the mean of Π . (b) Theoretical values for perfect state preparation and measurement. The curve is the ideal value of the mean as a function of ϕ , and error bars give the ideal variance.

conspiracy between detectors. In this sense our experiment is complementary to the photon experiments.

This experiment gave the first violation of the Bell inequality for massive particles obtained using a complete set of correlation measurements. A previous experiment using protons [51] deduced a violation from an incomplete set of measurements using quantum mechanical assumptions. Furthermore, our data used the outcome of every shot of the experiment, so the violation is obtained without the use of the fair-sampling hypothesis, closing the detector loophole for the first time. However, the ‘locality loophole’ remains open for our data. Since the detection events on the two ions occur within each other’s lightcones, in principle the detections could influence each other, leading to spurious correlations.

8. Sub-shot-noise interferometry

Frequency measurements using atomic clocks are currently the most accurate measurements of any physical quantity [63–65]. These clocks measure the transition frequency between two electronic levels $|\downarrow\rangle$ and $|\uparrow\rangle$ of an atomic sample to derive a stable reference for a local oscillator (LO). The LO usually interrogates the transition by Ramsey spectroscopy [66]. The simplest variant of this method consists of three steps: (1) the LO applies a $\pi/2$ rotation to the atoms, (2) the atoms undergo free evolution for a time T_R and (3) the LO again applies a $\pi/2$ rotation. In the frame rotating at the LO frequency, the free evolution (step 2) causes the part of the atomic state in $|\uparrow\rangle$ to acquire a phase ϕ_R relative to the part of the state in $|\downarrow\rangle$ and measuring the atomic spin state gives

$$\langle J_z \rangle = N(1 - \cos \phi_R)/2. \quad (20)$$

Because of the finite number of atoms involved, shot noise limits the minimum detectable phase shift to $\phi_{\text{shot}} = 1/\sqrt{N}$.

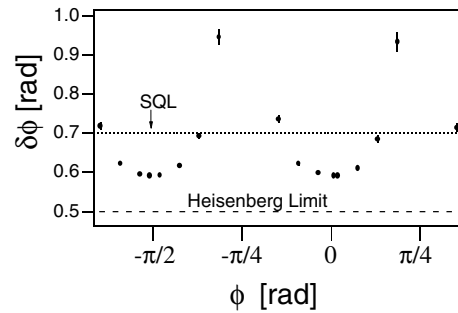


Figure 13. Measurement uncertainty $\delta\phi$ derived from the data of figure 12(a). For certain values of ϕ the uncertainty drops below the SQL, demonstrating SSN interferometry.

States that exhibit quantum correlations allow estimates of ϕ with smaller uncertainty than the shot-noise limit [14, 67–70]. Such sub-shot-noise (SSN) interferometry was first demonstrated using squeezed light [71, 72], and later using pairs of entangled photons [73]. Recently Orzel *et al* [74] have claimed reduction of the atom number variance in a collection of Bose–Einstein condensates, a step toward realizing SSN interferometry with matter waves. The analogue of SSN interferometry in atomic spin systems uses entangled spin states to improve phase estimation [14]. In particular, using SSN interferometry to measure ϕ can lead to improved frequency standards [14, 42, 75, 76]. Though two experiments using atomic spins [77, 78] have reduced the spin noise below the value expected for uncorrelated atoms, these experiments did not apply the squeezing to interferometry.

Using entangled states of two ions, we surpassed the phase precision limit for an ideal experiment with two uncorrelated ions, showing that SSN interferometry is indeed possible [14]. Following the scheme of Bollinger and Wineland [42, 75, 76], we prepared the state $|\downarrow\downarrow\rangle + |\uparrow\uparrow\rangle$, performed a $\pi/2$ rotation at phase ϕ and measured the value of the parity operator $\Pi = S_{1,z}S_{2,z}$ over 10 000 shots. Figure 12(a) shows the observed mean $\langle \Pi \rangle$ and variance $(\Delta\Pi)^2$ of the parity as a function of ϕ . For comparison, figure 12(b) shows the expected mean and variance for a perfect input state $|\downarrow\downarrow\rangle + |\uparrow\uparrow\rangle$ and ideal rotation and detection. The imperfect preparation of the entangled state significantly increases the variance for $|\langle \Pi \rangle| \sim 1$, but the quantum noise clearly dominates for $|\langle \Pi \rangle| \sim 0$. We can directly derive the uncertainty $\delta\phi$ from the data using standard quantum measurement theory [14]. Figure 13 shows these derived values of $\delta\phi$ as a function of ϕ . While the technical noise increases $\delta\phi$ well above the SQL for $|\langle \Pi \rangle| \sim 1$, $\delta\phi$ drops significantly below the SQL for $|\langle \Pi \rangle| \sim 0$. The minimum value of $\delta\phi$ is $0.59 \pm 0.01 < 1/\sqrt{2}$, giving an improvement in signal-to-noise of 1.20 ± 0.01 beyond the shot-noise limit.

Although our experiment showed only modest gains in signal-to-noise over the shot-noise limit, one can use the same scheme with large entangled states $|\downarrow^N\rangle + |\uparrow^N\rangle$ to achieve the fundamental limit to phase estimation $\delta\phi = 1/N$ [42, 75, 76]. For large N this uncertainty is a vast improvement over the shot-noise limit $\delta\phi = 1/\sqrt{N}$, allowing corresponding improvements in atomic clocks. Our scheme is closely related to the dual Fock-state scheme considered in optical and matter-wave interferometry [73, 79–83], and in fact coincides with it for two particles, so our measurement also provides a proof of principle for this method.

9. A decoherence-free quantum memory

Large-scale quantum computers will require robust long-term storage of quantum information [84], but a multitude of decoherence mechanisms stand in the way of a reliable quantum memory. In a classical computer, one usually evades memory errors by storing backup copies of information. However, the destructive nature of quantum measurement makes it impossible to reliably copy quantum information [85], so we must resort to other methods.

Collective decoherence processes, which have the same effect on each qubit, are expected to cause decay of many proposed quantum memories [86–92]. In fact, the most prominent decoherence mechanism in our experiment is the collective dephasing caused by fluctuating magnetic fields. Since the ion string is very small compared to the spatial wavelength of these magnetic fields, the Hamiltonian for this process is just proportional to J_z . States of the quantum register with the same number of spins up are degenerate under this Hamiltonian and are said to form a DFS of the full Hilbert space; any superposition of states in the DFS is unaffected by the decoherence process.

The space spanned by $|\downarrow\uparrow\rangle$ and $|\uparrow\downarrow\rangle$ is the simplest example of a DFS [90–92]. Since this space contains two states, we can encode one qubit’s worth of information into this DFS. We have experimentally demonstrated encoding of a qubit into this DFS and shown that the encoded qubit resists collective dephasing. Although we have discussed only the coupling to magnetic field, encoding into the DFS protects against any dephasing mechanism that acts in the same way on all qubits. In particular, our data show the resistance of the DFS to collective dephasing originating from either a fluctuating magnetic field or a fluctuating uniform Stark shift.

Generic DFSs have been shown to support fault-tolerant QC [93, 94]. Moreover, a generic DFS is robust to small perturbations that break the collective symmetry; transitions between the DFS and the rest of the Hilbert space are suppressed to first order [93]. As a robust, low-overhead way to remove the ubiquitous collective decoherence, DFSs will most likely be intrinsic to future QC architectures. The entangling gate demonstrated above enables universal quantum computation on qubits encoded in the DFS [13]. While a recent experiment has observed resistance of the singlet state of two photons to collective noise [95], a DFS of at least two states is required to encode a qubit. Our experiment encoded a qubit into a DFS for the first time.

Our encoding method reversibly maps an arbitrary state of one ion onto the DFS spanned by the states $|\Psi_{\pm}\rangle = |\downarrow\uparrow\rangle \pm |\uparrow\downarrow\rangle$, which is the same as the DFS over $|\downarrow\uparrow\rangle, |\uparrow\downarrow\rangle$ discussed above. The sequence of operations used to demonstrate encoding is given in table 4. Here a ‘block’ denotes a group of operations that jointly perform a quantum logic task. The first Ramsey block prepared the bare state $|\Psi_{\text{bare}}(\alpha)\rangle = |\downarrow\rangle \otimes (|\downarrow\rangle - ie^{i\alpha}|\uparrow\rangle)$ by rotating the spin of one ion while leaving the other ion alone. We refer to the ion rotated by the first Ramsey block as ion 2. In the bare state, the quantum information was carried by ion 2 alone. The encoding block mapped $|\Psi_{\text{bare}}(\alpha)\rangle$ to the DFS-encoded state $|\Psi_{\text{DFS}}(\alpha)\rangle = |\Psi_{-}\rangle + e^{i\alpha}|\Psi_{+}\rangle$, in which the information was carried jointly in the DFS states of the two ions. We allowed

the encoded state to evolve freely for a short time (usually $\sim 20 \mu\text{s}$), then decoded it by performing the inverse of the unitary evolution applied by the encoding block. Decoding nominally returned the register to the bare state $|\Psi_{\text{bare}}(\alpha)\rangle$. Finally, the second Ramsey block rotated ion 2 alone about an axis specified by β .

Ignoring the encoding and decoding blocks for a moment, we see that the two Ramsey blocks just implemented Ramsey spectroscopy on ion 2. Sweeping β and detecting $\langle J_z \rangle$ gave rise to the usual Ramsey fringes (equation (20)), but with a constant offset in $\langle J_z \rangle$, since ion 1 always remained in the state $|\downarrow\rangle$. The amplitude of the Ramsey fringes nominally measured the coherence remaining in the state of ion 2 just before the second Ramsey block. Since the encoding and decoding blocks together amounted to just the identity operator, we could measure the coherence of the encoded state from the amplitude of the Ramsey fringes.

To perform a Ramsey block, we individually addressed the ions using the RF phase and trap voltage. In a classical picture of spin, the first rotation (e.g., step 1 in table 4) took $\downarrow\downarrow$ to $\searrow\searrow$. The second rotation (e.g., step 2) reversed the sense of rotation on ion 1, while keeping it the same on ion 2, so the second rotation took $\searrow\searrow$ to $\downarrow\rightarrow$. This procedure rotated ion 2 alone, without changing the state of ion 1. The phase α was just set by the RF phase. More generally, two rotations by θ at these ion phases generated the state $\cos 2\theta|\downarrow\rangle - ie^{i\alpha}\sin 2\theta|\uparrow\rangle$.

To encode the bare state into the DFS, we first applied the entangling gate three times (step 3 of table 4) by tripling the usual entangling pulse duration, nominally obtaining the evolution U_{ent}^{-1} . This operation mapped the part of the bare state in $|\uparrow\rangle$ into the DFS state $|\Psi_{+}\rangle$. The phases of the subsequent $\pi/2$ pulse (step 4) were set so that this pulse had no effect on $|\Psi_{+}\rangle$, but mapped the state $|\downarrow\downarrow\rangle + i|\uparrow\uparrow\rangle$ resulting from the entangling operation into the orthogonal DFS state $|\Psi_{-}\rangle$.

After waiting a minimum of $\sim 25 \mu\text{s}$, we decoded the DFS state by applying the operator inverse of the encoding block. First we applied another $\pi/2$ pulse with the rotation axes of both ions reversed, corresponding to a change in the RF phase by π . The trap voltage was kept at V_3 throughout steps 4–6 to save settling time. We then changed the trap voltage to V_1 and applied the usual entangling gate. We had to apply the entangling gate three times to obtain its inverse, so the error of the inverse gate was three times that of the usual gate. The gate error increased due to heating, and this error would have tripled if we had used the usual gate in the encoding and the inverse gate in the decoding. The decoding block took $15 \mu\text{s}$ to complete. After decoding, the second Ramsey block and the detection produced the Ramsey fringes that constituted our signal.

We built up a histogram at each step of β from 1000 shots of the experiment. We constructed reference histograms from the data averaged over β and used these references to deduce the value of P_i at each step of β . Ion 2 typically scattered about 10% more photons in $|\downarrow\rangle$ than ion 1 did, presumably due to unequal illumination by BD. We therefore allowed the mean of the Poissonian for one ion bright to vary independently of the mean for two ions bright. The extra free parameter did not increase the error in determining P_i . We fit the data on $P_i(\beta)$ to sinusoids of amplitude \tilde{P}_i . The error in \tilde{P}_i was typically 0.05–0.08.

Table 4. The sequence of operations used to demonstrate DFS encoding. Rotations by an angle θ are written $U_{\text{car}}(\theta)$. ‘Block’ refers to a group of operations that jointly perform a quantum logic task. A Ramsey block performs a $\pi/2$ rotation on ion 2 while leaving ion 1 alone. The encoding and decoding blocks map the information in ion 2 into and out of the DFS spanned by $|\Psi_{-}\rangle$, $|\Psi_{+}\rangle$. We specify some intermediate register states for clarity.

Number	Block	Operation	ϕ_1	ϕ_2	State after operation
0	Initialize	—	—	—	$ \downarrow\downarrow\rangle$
1	Ramsey	$U_{\text{car}}(\pi/4)$	α	α	—
2		$U_{\text{car}}(\pi/4)$	$\alpha + \pi$	α	$ \downarrow\rangle \otimes (\downarrow\rangle - ie^{i\alpha} \uparrow\rangle)$
3	Encode	U_{ent}^{-1}	0	0	$(\downarrow\downarrow\rangle + i \uparrow\uparrow\rangle) - e^{i\alpha} \Psi_{+}\rangle$
4		$U_{\text{car}}(\pi/2)$	$\pi/2$	0	$ \Psi_{-}\rangle + e^{i\alpha} \Psi_{+}\rangle$
5	Wait	—	—	—	—
6	Decode	$U_{\text{car}}(\pi/2)$	$3\pi/2$	π	$(\downarrow\downarrow\rangle + i \uparrow\uparrow\rangle) - e^{i\alpha} \Psi_{+}\rangle$
7		U_{ent}	0	0	$ \downarrow\rangle \otimes (\downarrow\rangle - ie^{i\alpha} \uparrow\rangle)$
8	Ramsey	$U_{\text{car}}(\pi/4)$	$\alpha + \beta$	$\alpha + \beta$	—
9		$U_{\text{car}}(\pi/4)$	$\alpha + \beta + \pi$	$\alpha + \beta$	$ \downarrow\rangle \otimes \left(\sin \frac{\beta}{2} \downarrow\rangle - ie^{i\beta} \cos \frac{\beta}{2} \uparrow\rangle \right)$
10	Detect	—	—	—	—

To determine the fidelity of the encoding/decoding sequence, we compared data taken with the encoding and decoding (‘DFS data’) to data taken without these operations (‘bare data’). Dead time was substituted for the encoding/decoding operations in the latter case, so that the time between Ramsey blocks was the same in both cases. Ideally $\tilde{P}_0 = 0$, but in practice $P_0(\beta)$ oscillated appreciably in the data. For the bare data we found $\tilde{P}_0 \lesssim 0.04$, showing that the presumed individual rotation of ion 2 actually affected ion 1 as well. The two rotations composing a Ramsey block were therefore identical up to a gate error of ~ 0.02 . For the DFS data we found $\tilde{P}_0 \lesssim 0.10$. P_1 and P_2 oscillated π out of phase with P_0 in both cases and we found $\tilde{P}_2 = \tilde{P}_0 + \tilde{P}_1$ within error. We characterized each dataset by the coherence $C = \tilde{P}_2$. For the bare data we found $C_{\text{bare}} = 0.69 \pm 0.08$, while for the DFS data we found $C_{\text{DFS}} = 0.43 \pm 0.05$. The loss of contrast of the bare data mostly comes from the decoherence of the bare state over the $\sim 100 \mu\text{s}$ delay between the two Ramsey blocks, as well as from the gate error, which we estimate as ~ 0.04 for each Ramsey block. We expect the population decay to be smaller than the decay of the coherence, so we can set a lower limit for the encoding/decoding fidelity as $F_{\text{encode}} \gtrsim C_{\text{DFS}}/C_{\text{bare}} = 0.62$. The errors in encoding and decoding mostly come from errors in the entangling operations.

The operations in the Ramsey blocks (steps 1, 2, 8 and 9) were thus all mutually coherent, as were the encoding and decoding sequences (steps 3, 4, 6 and 7). However, the encoding/decoding blocks were not coherent with the Ramsey blocks, since the synthesizer frequencies between the two blocks differed by the Stark shift ($\sim 7 \text{ kHz}$). In a frame rotating at the beat frequency of step 4, the bare state phase α precesses at $\sim 7 \text{ kHz}$, so the data were effectively averaged over the bare state phase. The persistence of the coherence under these conditions shows that the encoding procedure works even if we do not know the bare state phase. It is then no stretch of credulity to suppose that the encoding procedure works for an arbitrary superposition of $|\downarrow\rangle$ and $|\uparrow\rangle$.

To study the effects of decoherence on the DFS-encoded state, we engineered a collective dephasing environment using an off-resonant laser beam with a randomly varying intensity.

The beam induces shifts of $\omega_{\downarrow\uparrow}$ that are common to both ions through the AC Stark effect. The DFS state should resist the dephasing effect of this environment. The coherence of ion 2 in the test state $|\downarrow\rangle(|\downarrow\rangle + e^{i\phi}|\uparrow\rangle)/\sqrt{2}$, however, should be sensitive to collective dephasing. We measure the decay of the test state by simply turning off the encoding and decoding sequences in the procedure used to measure the decay of the DFS-encoded state. We applied the noise beam to the test state and encoded state during a delay time of about $25 \mu\text{s}$, as shown in figure 14. The coherence without applied noise is about 0.69 for the test state and about 0.43 for the encoded state; they depart from unity because of imperfect logic gates and detection. For white-noise intensity fluctuations of the Stark-shifting beam, we expect C to decay exponentially for the test state, as shown by the fit line. We also fit the coherence of the DFS state to an exponential decay for comparison. The decay rate of the test state is $0.18(1) \mu\text{s}^{-1}$, while the decay rate of the DFS state is $0.0035(50) \mu\text{s}^{-1}$, consistent with zero decay.

We have also measured the storage times of the encoded and test states under ambient conditions in our laboratory. The data are shown in figure 15. Here we leave a variable delay time between encoding and decoding to give the ambient noise time to act. The decoherence of the test state is dominated by ambient fluctuating magnetic fields whose frequencies lie primarily at 60 Hz and its harmonics. These fields randomly shift $\omega_{\downarrow\uparrow}$ through the Zeeman effect. Since these fields are roughly uniform across the ion string, they induce collective dephasing similar to that created by the engineered environment. We empirically find the decay of both test and encoded states to be roughly exponential, as indicated by the fit lines. The decay rate of the test state is $7.9(1.5) \times 10^{-3} \mu\text{s}^{-1}$, while the decay rate of the DFS state is $2.2(0.3) \times 10^{-3} \mu\text{s}^{-1}$. The long lifetime of the DFS state shows that collective dephasing from magnetic field noise is the major ambient source of decoherence for the test state. The loss of coherence of the encoded state is consistent with degradation of the decoding pulses [25, 41] due to heating of the ion motional state over the delay time [31].

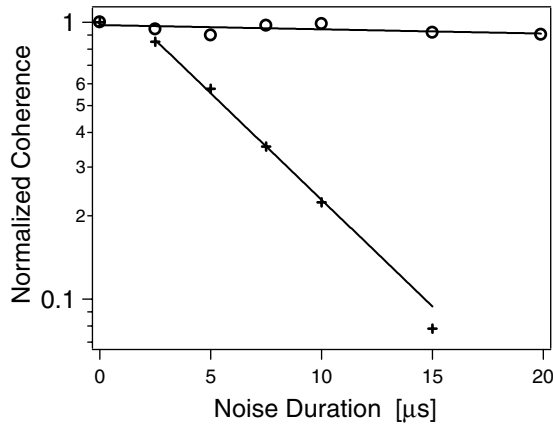


Figure 14. Decay of DFS-encoded state (circles) and test state (crosses) under engineered dephasing noise. The noise is applied for a fraction of the delay time of about $25 \mu\text{s}$ between encoding and decoding. Coherence data are normalized to their values for zero applied noise. The fit lines are exponential decay curves. The DFS data are fitted for comparison.

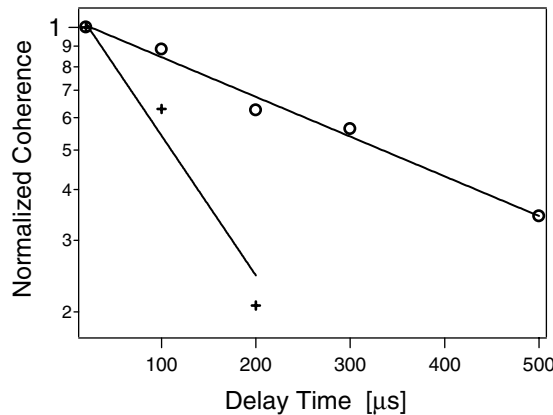


Figure 15. Decay of DFS-encoded state (circles) and test state (crosses) under ambient decoherence. We vary the delay time between encoding and decoding to give the ambient noise a variable time to act. Coherence data are normalized to their values for zero delay time. The fit lines are exponential decay curves for purposes of comparison and are not theoretical predictions.

10. Toward large-scale ion trap quantum computing

As we have seen, one can use a small number of trapped ions to construct a quantum register. However, manipulating a large number of ions in a single trap presents immense technical difficulties, and scaling arguments suggest that a single trap can only support computations on tens of ions [25, 96, 97]. To build up a large-scale ion trap quantum computer, one can envision quantum communication between a number of small ion-trap quantum registers. Recent proposals along these lines using photon coupling [98, 99] and spin-dependent Coulomb interactions [100] rely on untested methods of quantum state manipulation. Here we present a scheme using only quantum manipulation techniques that have already been experimentally demonstrated.

To build up a large-scale quantum computer, we proposed [13] a ‘quantum charge-coupled device’ (QCCD) architecture consisting of a large number of interconnected ion traps. By changing the operating voltages of these traps,

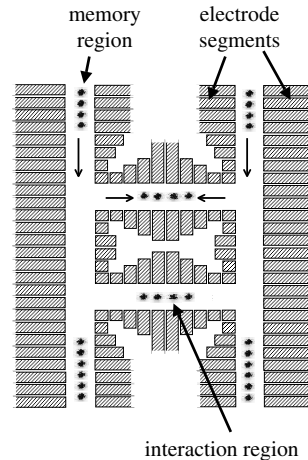


Figure 16. Schematic of the QCCD. Ions are stored in the memory region and moved to the interaction region for logic operations. Thin arrows show transport and confinement along the local trap axis.

we can confine a few ions in each trap or shuttle ions from trap to trap. In any particular trap, we can manipulate a few ions using the methods already demonstrated, while the connections between traps allow communication between sets of ions [25]. Since both the speed of quantum logic gates [101] and the shuttling speed are limited by the trap strength, shuttling ions between memory and interaction regions should consume an acceptably small fraction of a clock cycle.

Figure 16 shows a schematic of the proposed device. Trapped ions storing quantum information are held in the memory region. To perform a logic gate, we move the relevant ions into an interaction region by applying appropriate voltages to the electrode segments. In the interaction region, the ions are held close together, enabling the Coulomb coupling necessary for entangling gates [35, 41]. Lasers are focused through the interaction region to drive gates. We then move the ions again to prepare for the next operation.

We can realize the trapping and transport potentials needed for the QCCD using a combination of radiofrequency (RF) and quasistatic electric fields. Figure 16 shows only the electrodes that support the quasistatic fields. By varying the voltages on these electrodes, we can perform ion transport and confinement along the local trap axis, which lies along the arrows in figure 16. Two more layers of electrodes lie above and below the static electrodes. Applying RF voltage to the outer layers confines the ions transverse to the local trap axis, just as for the standard linear trap. This geometry allows stable transport of the ions around T- and X-junctions, so we can build complex, multiply connected trap structures.

A first step toward a QCCD has been taken at NIST by constructing a pair of interconnected ion traps; the individual traps are similar to those used in previous work [31] and are separated by 1.2 mm. Efficient coherent transport of a qubit between the two traps was demonstrated by performing a Ramsey-type experiment involving the two traps, where the high contrast indicated coherence transfer [102]. Transport times were as short as $\sim 20 \mu\text{s}$, with corresponding ion velocities greater than 50 m s^{-1} (see also [103]). The transport did not cause any shortening of trap lifetime.

To maximize the clock speed of the QCCD, we will need to transport ions quickly. However, the entangling

gate demonstrated in previous work at NIST [10, 41] has low error only for ions cooled near the quantum ground state. To recool the ions after transport and to counteract the effects of heating [31], we propose to use sympathetic cooling of the ions used for quantum logic by another ion species [19, 25, 104]. Confining both species in the interaction region lets us use the cooling species as a heat sink, with the Coulomb interaction providing energy transfer between the two species, as experimentally demonstrated in [105–107].

While the decoherence and gate errors in single-trap quantum registers have already been characterized, additional decoherence can occur during ion transport. For instance, the energy splitting of the qubit states of an ion depends on the magnetic field at the ion through the Zeeman effect. During ion transport, the spatial variations of the magnetic field strength along the transport path cause the qubit states to acquire a path-dependent relative phase α , so that, e.g., $|\downarrow\rangle + |\uparrow\rangle \rightarrow |\downarrow\rangle + e^{i\alpha}|\uparrow\rangle$ over transport. If we do not know α , we have lost the phase information, effectively dephasing the quantum state. But knowing α for all relevant paths is tantamount to characterizing the magnetic field on micron length scales across the entire device, a very difficult task.

Retaining phase information during a computation also requires accurate positioning of the ions in the interaction regions. Since the logic gate parameters depend on the phase of the driving laser fields at the ion positions, the ion positions and laser path lengths must be controllable with accuracies much better than an optical wavelength. While this does not place unreasonable constraints on the accuracy of the voltage sources driving the QCCD electrodes, stray electric fields emanating from the electrodes or mechanical vibration of the QCCD can readily move the ions a fraction of a wavelength from their nominal positions, effectively adding a relative phase α of the type considered above.

Both these types of decoherence produce collective dephasing, so we can eliminate them by encoding each qubit into the DFS described above. As an example, assume that the physical qubit energies have a linear dependence on magnetic field and that the field varies linearly over an extended QCCD device of size 10 cm. If we assume each pair of qubits comprising a logical qubit is separated on average by 10 μm , we expect a reduction in dephasing for two widely separated qubits by a factor of 10^4 when encoded in the DFS. We can make similar arguments for any external-field shift of the qubit energy splitting, for instance Stark shifts of the qubit levels induced by the electric fields that push the ions from place to place.

We can also perform universal quantum logic in the DFS. As shown in [13, 108], the two-ion entangling gate performs a rotation on a single logical qubit, while the four-ion gate performs an entangling operation on a pair of logical qubits. To use the DFS encoding in a large-scale quantum computation, we initialize the ions in pairs to the state $|\downarrow\uparrow\rangle$. Each pair of ions remains in the DFS throughout the quantum computation, so the logical qubits resist transport decoherence and all other types of collective dephasing. Readout of the DFS qubit is straightforward, since we need only discriminate between $|\downarrow\uparrow\rangle$ and $|\uparrow\downarrow\rangle$. Notably, all logic gate operations can be accomplished by uniformly illuminating the ions in the interaction region, removing the need for tightly focused laser beams.

The DFS encoding also removes the requirement of clock synchronization between logic gates, a major but

little-recognized obstacle to large-scale parallel quantum computation. Since the energy levels of our physical qubits are nondegenerate, we must keep track of the resulting phase accumulation to preserve the quantum information in the physical qubit basis [7]. Parallel operations taking place in many interaction regions thus require clocks that remain synchronized over the whole computation time [109]. Synchronization can become very difficult for many qubits: for a transition frequency $\omega_{\downarrow\uparrow}$ between $|\downarrow\rangle$ and $|\uparrow\rangle$, the two components of the state $|\downarrow\rangle^N + |\uparrow\rangle^N$ acquire a significant relative phase in a time $\sim 1/(N\omega_{\downarrow\uparrow})$. To maintain phase stability of the computation, we therefore require a frequency reference with fractional frequency stability much better than $\lesssim 1/(N\omega_{\downarrow\uparrow}\tau)$ at an averaging time τ equal to the length of the quantum computation.

To be concrete, we consider trapped $^{40}\text{Ca}^+$ ions as qubits, with the ground $S_{1/2}$ state and metastable $D_{5/2}$ states as logic levels. This system is being investigated for quantum computation by a number of groups [5, 97, 101]. Here the transition frequency is 412 THz, comparable to the 533 THz operating frequency of the currently most stable laser oscillator [110], which has a fractional frequency instability of 3×10^{-16} at 1 s averaging time. If the computation takes about 1 s, equal to the lifetime of the metastable $D_{5/2}$ state, we see that current technology fails to provide the appropriate phase stability for even one ion. The situation is even worse if we require this level of synchronization between spatially separated regions. However, since the logic levels of a DFS-encoded qubit are degenerate, we do not need phase synchronization to perform a logic operation *within* the DFS. The universal gate-set constructed above allows us to perform highly parallel computations in the DFS without synchronization between gates separated in time or space. Similar considerations would apply to other QC architectures.

We have presented a realistic architecture for quantum computation that is scalable to large numbers of qubits. In contrast to other proposals, all local quantum state manipulations necessary for our scheme have already been experimentally tested in small quantum registers, and scaling up to large ion-trap quantum computers appears straightforward.

11. Conclusion

We have demonstrated four-particle entanglement, violation of Bell's inequality, SSN phase estimation and encoding into a DFS using a small quantum register of trapped ions. While these experiments are important steps on the road to quantum computation, the major challenge remains: scaling up the techniques developed for a few ions to build a large-scale quantum computer with thousands or millions of qubits. Fortunately, we have a plausible roadmap to our goal, the 'quantum CCD' model of ion-trap QC.

References

- [1] Shor P 1994 *Proc. 35th Ann. Symp. on the Foundations of Computer Science* (Los Alamitos, CA: IEEE Computer Society Press) p 116
- [2] Grover L 1997 *Phys. Rev. Lett.* **79** 325
- [3] Diedrich F, Bergquist J, Itano W and Wineland D 1989 *Phys. Rev. Lett.* **62** 403

- [4] King B *et al* 1998 *Phys. Rev. Lett.* **81** 1525
- [5] Roos C *et al* 1999 *Phys. Rev. Lett.* **83** 4713
- [6] Rowe M *et al* 2001 *Nature* **409** 791
- [7] Kielpinski D *et al* 2001 *Science* **291** 1013
- [8] Itano W *et al* 1993 *Phys. Rev. A* **47** 3554
- [9] Schmidt-Kaler F *et al* 2000 *J. Mod. Opt.* **47** 2573
- [10] Sackett C *et al* 2000 *Nature* **404** 256
- [11] Monroe C *et al* 1995 *Phys. Rev. Lett.* **75** 4714
- [12] Nägerl H *et al* 1999 *Phys. Rev. A* **60** 145
- [13] Kielpinski D, Monroe C and Wineland D 2002 *Nature* **417** 709
- [14] Meyer V *et al* 2001 *Phys. Rev. Lett.* **86** 5870
- [15] Raizen M *et al* 1992 *J. Mod. Opt.* **39** 233
- [16] Ghosh P 1995 *Ion Traps* (Oxford: Clarendon)
- [17] Steane A 1997 *Appl. Phys. B* **64** 623
- [18] James D 1998 *Appl. Phys. B* **66** 191
- [19] Kielpinski D *et al* 2000 *Phys. Rev. A* **61** 032310
- [20] Arimondo E 1996 *Progress in Optics* vol 35 (Amsterdam: Elsevier) p 259
- [21] Dehmelt H 1975 *Bull. Am. Phys. Soc* **20** 60
- [22] Wineland D, Bergquist J, Itano W and Drullinger R 1980 *Opt. Lett.* **5** 245
- [23] Nagourney W, Sandberg J and Dehmelt H 1986 *Phys. Rev. Lett.* **56** 2797
- [24] King B 1999 *PhD Thesis* University of Colorado available at <http://jilawww.colorado.edu/www/sro/thesis/king/index.html>
- [25] Wineland D *et al* 1998 *J. Res. NIST* **103** 259
- [26] Kielpinski D 2001 *PhD Thesis* University of Colorado available at <http://www.boulder.nist.gov/timefreq/ion/qucomp/papers.htm>
- [27] Wineland D and Itano W 1979 *Phys. Rev. A* **20** 1521
- [28] Monroe C *et al* 1995 *Phys. Rev. Lett.* **75** 4011
- [29] Dicke R 1953 *Phys. Rev.* **89** 472
- [30] Bergquist J, Itano W and Wineland D 1987 *Phys. Rev. A* **36** 428
- [31] Turchette Q *et al* 2000 *Phys. Rev. A* **61** 063418
- [32] Deutsch D, Barenco A and Ekert A 1995 *Proc. R. Soc. A* **449** 669
- [33] Lloyd S 1995 *Phys. Rev. Lett.* **75** 346
- [34] Barenco A *et al* 1995 *Phys. Rev. A* **52** 3457
- [35] Cirac J and Zoller P 1995 *Phys. Rev. Lett.* **74** 4091
- [36] Turchette Q *et al* 1995 *Phys. Rev. Lett.* **75** 4710
- [37] Rauschenbeutel A *et al* 1999 *Phys. Rev. Lett.* **83** 5166
- [38] Sørensen A and Mølmer K 1999 *Phys. Rev. Lett.* **82** 1971
- [39] Mølmer K and Sørensen A 1999 *Phys. Rev. Lett.* **82** 1835
- [40] Cohen-Tannoudji C, Dupont-Roc J and Grynberg G 1992 *Atom-Photon Interactions* (New York: Wiley)
- [41] Sørensen A and Mølmer K 2000 *Phys. Rev. A* **62** 022311
- [42] Bollinger J, Wineland D, Itano W and Heinzen D 1996 *Phys. Rev. A* **54** 4649
- [43] Dür W and Cirac J 2001 *J. Phys. A: Math. Gen.* **34** 6837
- [44] Wootters W 1998 *Phys. Rev. Lett.* **80** 2245
- [45] Bennett C *et al* 1996 *Phys. Rev. Lett.* **76** 722
- [46] Lewenstein M *et al* 2000 *J. Mod. Opt.* **47** 2481
- [47] Vedral V and Plenio M 1998 *Phys. Rev. A* **57** 1619
- [48] Einstein A, Podolsky B and Rosen N 1935 *Phys. Rev.* **47** 777
- [49] Bell J 1965 *Physics (NY)* **1** 195
- [50] Freedman S and Clauser J 1972 *Phys. Rev. Lett.* **28** 938
- [51] Laméhi-Rachti M and Mittag W 1976 *Phys. Rev. D* **14** 2543
- [52] Aspect A, Grangier P and Roger G 1982 *Phys. Rev. Lett.* **49** 91
- [53] Aspect A, Dalibard J and Roger G 1982 *Phys. Rev. Lett.* **49** 1804
- [54] Weihs G *et al* 1998 *Phys. Rev. Lett.* **81** 5039
- [55] Zbinden H, Brendel J, Gisin N and Tittel W 2001 *Phys. Rev. A* **63** 022111
- [56] Bohm D 1952 *Phys. Rev.* **85** 166
- [57] Bohm D 1952 *Phys. Rev.* **85** 180
- [58] Clauser J, Horne M, Shimony A and Holt R 1969 *Phys. Rev. Lett.* **23** 880
- [59] Clauser J and Horne M 1974 *Phys. Rev. D* **10** 526
- [60] Eberhard P 1993 *Phys. Rev. A* **47** 747
- [61] Richter T 1983 *Opt. Acta* **30** 1769
- [62] Eichmann U *et al* 1993 *Phys. Rev. Lett.* **70** 2359
- [63] Bergquist J (ed) 1996 *Proc. 5th Conf. on Frequency Standards and Metrology* (Singapore: World Scientific)
- [64] Sullivan D *et al* 2001 *J. Res. NIST* **106** 47
- [65] Udem T *et al* 2001 *Phys. Rev. Lett.* **86** 4996
- [66] Ramsey N 1963 *Molecular Beams* (London: Oxford University Press)
- [67] Yurke B, McCall S and Klauder J 1986 *Phys. Rev. A* **33** 4033
- [68] Caves C 1981 *Phys. Rev. D* **23** 1693
- [69] Kitagawa M and Ueda M 1993 *Phys. Rev. A* **47** 5138
- [70] Walls D and Milburn G 1994 *Quantum Optics* (New York: Springer)
- [71] Xiao M, Wu L and Kimble H 1987 *Phys. Rev. Lett.* **59** 278
- [72] Grangier P, Slusher R, Yurke B and LaPorta A 1987 *Phys. Rev. Lett.* **59** 2153
- [73] Kuzmich A and Mandel L 1998 *Quantum Semiclass. Opt.* **10** 493
- [74] Orzel C *et al* 2001 *Science* **291** 2386
- [75] Wineland D *et al* 1992 *Phys. Rev. A* **46** 6798
- [76] Wineland D, Bollinger J, Itano W and Heinzen D 1994 *Phys. Rev. A* **50** 67
- [77] Hald J, Sorensen J L, Schori C and Polzik E S 1999 *Phys. Rev. Lett.* **83** 1319
- [78] Kuzmich A, Mandel L and Bigelow N 2000 *Phys. Rev. Lett.* **85** 1594
- [79] Holland M and Burnett K 1993 *Phys. Rev. Lett.* **71** 1355
- [80] Bouyer P and Kasevich M 1997 *Phys. Rev. A* **56** 1083
- [81] Kim T *et al* 1998 *Phys. Rev. A* **57** 4004
- [82] Sanders B and Milburn G 1995 *Phys. Rev. Lett.* **75** 2944
- [83] Kim T *et al* 1998 *Opt. Commun.* **156** 37
- [84] Steane A 2003 *Proc. 5th Int. Conf. on Quantum Communication, Measurement, and Computing (Capri)* at press
- [85] Wootters W and Zurek W 1982 *Nature* **299** 802
- [86] Palma G, Suominen K-A and Ekert A 1996 *Proc. R. Soc. A* **452** 567
- [87] Zanardi P and Rossi F 1998 *Phys. Rev. Lett.* **81** 4752
- [88] 1998 *Fortschr. Phys.* **46** special issue 4–5, 329–589
- [89] 2000 *Fortschr. Phys.* **48** special issue 9–11, 769–1138
- [90] Lidar D, Chuang I and Whaley K 1998 *Phys. Rev. Lett.* **81** 2594
- [91] Zanardi P and Rasetti M 1997 *Phys. Rev. Lett.* **79** 3306
- [92] Duan L and Guo G 1998 *Phys. Rev. A* **57** 737
- [93] Lidar D, Bacon D and Whaley K 1999 *Phys. Rev. Lett.* **82** 4556
- [94] Bacon D, Kempe J, Lidar D and Whaley K 2000 *Phys. Rev. Lett.* **85** 1758
- [95] Kwiat P, Berglund A, Altepeter J and White A 2000 *Science* **290** 498
- [96] Hughes R *et al* 1996 *Phys. Rev. Lett.* **77** 3240
- [97] Enzer D 2001 *Experimental Implementation of Quantum Computation'01* (Princeton, NJ: Rinton)
- [98] Pellizzari T *et al* 1995 *Phys. Rev. Lett.* **75** 3788
- [99] DeVoe R 1998 *Phys. Rev. A* **58** 910
- [100] Cirac J and Zoller P 2000 *Nature* **404** 579
- [101] Steane A *et al* 2000 *Phys. Rev. A* **62** 042305
- [102] Rowe M *et al* 2002 *Quant. Info. Comput.* **2** 257
- [103] Guthöhrlein G *et al* 2001 *Nature* **414** 49
- [104] Morigi G and Walther H 2001 *Eur. Phys. J. D* **13** 261
- [105] Larson D *et al* 1986 *Phys. Rev. Lett.* **57** 70
- [106] Rohde H *et al* 2001 *J. Opt. B: Quantum Semiclass. Opt.* **3** S34
- [107] Blinov B *et al* 2002 *Phys. Rev. A* **65** 040304
- [108] Bacon D 2001 *PhD Thesis* University of California, Berkeley
- [109] van Enk S 2001 *J. Mod. Opt.* **48** 2049
- [110] Young B *et al* 1999 *Phys. Rev. Lett.* **82** 3799